

Numerical Simulation of a Laboratory Vortex

RICHARD ROTUNNO

National Center for Atmospheric Research¹, Boulder, Colo. 80307

(Manuscript received 21 June 1977, in revised form 11 August 1977)

ABSTRACT

An axisymmetric numerical model has been developed to simulate Ward's (1972) laboratory experiments. It was shown by Davies-Jones (1976) that this experiment is more geophysically relevant than all previous experiments in that Ward's experiment exhibits both dynamical and geometrical similarity to actual tornadoes.

Major results are 1) the core size versus inflow angle relationship agrees very nearly with Ward's measurements, 2) the numerical and laboratory surface pressure patterns are in agreement, and 3) it is demonstrated that the core radius is independent of the Reynolds number at high Reynolds number (Ward's data also exhibit this behavior).

Based on this axisymmetric model some speculation concerning the nature of the asymmetric multiple vortex phenomenon is made. Furthermore, the numerical model allows the examination of the interior flow field. As a consequence, an explanation is offered in Section 6 for the double-walled structure sometimes observed in natural vortices.

The experiments with no-slip boundary conditions reveal a very complicated flow structure in the vicinity of $r=z=0$. The computed flow field is strongly reminiscent of that described by Benjamin (1962).

1. Introduction

Laboratory models of atmospheric vortices date from the early 1950's. However, it is argued by Davies-Jones (1976) in a critical review of the subject that none of the early models are both dynamically and geometrically similar to natural vortices. Consider the vortex chamber in Fig. (1.1). According to Davies-Jones (1976), there are four independent nondimensional numbers which govern the flow. They are r_0/r_s , $h/r_0 \equiv a$ (the aspect ratio), $r_0 M / (2Q) \equiv S$ (the swirl ratio) and $Q / (vh) \equiv N$ (the radial Reynolds number). The quantities $2\pi Q$ and $2\pi M$ are the volume flow rate through the chamber and the circulation at the outer wall, respectively. The quantities r_0 , r_s and h are defined in Fig. (1.1). Davies-Jones (1973, 1976) comes to the conclusion that the experimental model of Ward (1972) obtains values of these quantities which agree with natural vortices better than any previous model. Ward's model also exhibits many features observed in natural vortices. Among these are a characteristic surface pressure pattern and multiple vortices.

An attempt to use numerical methods to study atmospheric vortices must be preceded by the successful simulation of the more controllable laboratory vortex. In view of the above discussion, it was decided the

simulation of Ward's (1972) experiment would prove to be a formidable test of both the physical concepts of the nature of the vortex and the numerical method.

An axisymmetric numerical model has been developed which gives results more in accord with Ward's data than previous modeling attempts. Specifically, 1) the core size versus inflow angle $[\arctan(v/u)_{r=r_s}]$ agree almost exactly with Ward's measurements, 2) the predicted surface pressure distributions are in near exact agreement with Ward's, and 3) it is demonstrated that the core radius is independent of the Reynolds number (N) at the high Reynolds number used (Ward's data also exhibit this behavior). It is impossible for the axisymmetric model to simulate the asymmetric multiple vortex phenomena. However, it has been suggested (Ward, 1972; Davies-Jones, 1973, 1976) that the multiple vortices arise as an instability on a cylindrical vortex sheet. The present model shows this cylindrical vortex sheet to be the solution as $N \rightarrow \infty$. All of these results are obtained using a free-slip lower boundary condition. A no-slip lower boundary condition induces a number of fascinating secondary flow features such as vortex breakdown, inertial waves on the column and inertial wave breaking.

2. Ward's model

Ward recognized that tornadoes typically occur within updrafts which are an order of magnitude larger than the funnel diameter (e.g., 10 km compared

¹ The National Center for Atmospheric Research is sponsored by the National Science Foundation.

to 0.5 km). Furthermore, the depth of the inflow layer which supplies the updraft is typically 2 km. Ward termed the ratio of the updraft diameter to the inflow depth the "configuration ratio" (twice the inverse aspect ratio defined above). This parameter exercises great control over the experimental results. The strength of Ward's model derives from the incorporation of "rising motion over an area appreciably greater in diameter than the depth of the converging layer." Hence, the geometry of the laboratory vortex could be made similar to actual tornadoes. Ward's model is also dynamically similar since Davies-Jones (1973) estimated the swirl ratio S for tornado cyclones to be $O(1)$ and this S is achieved by Ward's model. Although Reynolds number similarity is not achieved, this may be irrelevant since most of Ward's results are independent of N . (This result is confirmed by the numerical model.)

Ward's apparatus is shown in Fig. (2.1). There is a cylindrical chamber bounded above by a honeycomb grid over which suction is created by an exhaust fan. The rotating screen at the bottom imparts a specified amount of angular momentum to the in-rushing air. The honeycomb grid divorces the fan vortex from the flow in the chamber. The experiment possesses the advantage that the suction and screen rotation rate can be varied independently. Outlined in Fig. (2.1) is the area covered by the numerical model.

3. Mathematical model

The laboratory experiments show there is an axisymmetric regime for swirl ratios $S \lesssim 1$. The present model explores the flow in this regime. The governing equations are written under the restrictions of no azimuthal variations, constant density and viscosity. The momentum equations are (in cylindrical coordinates)

$$u_t + uu_r + wu_z - r^{-1}v^2 = -\rho^{-1}p_r + \nu\{[r^{-1}(ru)_r]_r + u_{zz}\}, \quad (3.1)$$

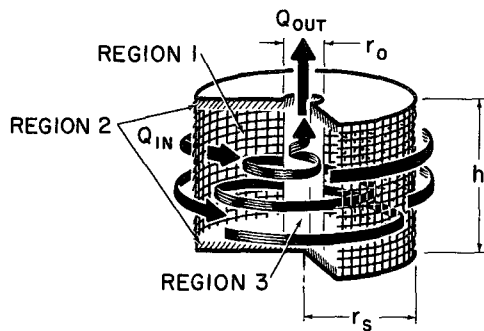


FIG. 1.1. A typical vortex chamber [concept after Lewellen (1971)]. Regions 1, 2 and 3 denote the outer flow, the top and bottom boundary layer regions and the core, respectively. The quantities r_o , r_s , h , Q_{in} and Q_{out} are the exhaust radius, inflow radius, inflow depth, volume inflow rate and volume outflow rate, respectively.

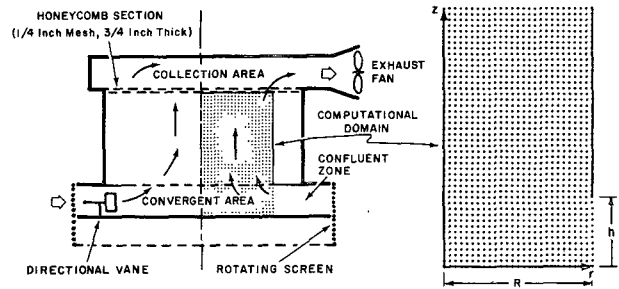


FIG. 2.1. Schematic of Ward's (1972) apparatus. The computational domain is indicated.

$$v_t + uv_r + wv_z + r^{-1}uv = \nu\{[r^{-1}(rv)_r]_r + v_{zz}\}, \quad (3.2)$$

$$w_t + uw_r + ww_z = -\rho^{-1}p_z + \nu[r^{-1}(rw_r)_r + w_{zz}]. \quad (3.3)$$

The conservation of mass equation is

$$r^{-1}(ru)_r + w_z = 0. \quad (3.4)$$

The quantities u , v , w , p and ν are the radial, azimuthal and vertical velocities, pressure and eddy viscosity, respectively. The independent variables are radius r , height z and time t . Subscripts denote partial differentiation. The radial, azimuthal and vertical components of the vorticity vector are

$$\xi = -v_z, \quad \eta = u_z - w_r, \quad \zeta = r^{-1}(rv)_r, \quad (3.5a,b,c)$$

respectively. A streamfunction ψ is defined such that

$$u = r^{-1}\psi_z, \quad w = -r^{-1}\psi_r. \quad (3.6a,b)$$

The circulation Γ is defined by

$$\Gamma = rv. \quad (3.7)$$

A convenient method for solving Eqs. (3.1)–(3.4) is to first form the governing equation for η . This is accomplished by combining the vertical derivative of Eq. (3.1) with the radial derivative of Eq. (3.3). Thus,

$$\eta_t - J(\psi, r^{-1}\eta) = r^{-3}(\Gamma^2)_z + \nu[(r^{-1}(r\eta)_r)_r + \eta_{zz}], \quad (3.8)$$

where $J(x, y) = x_r y_z - x_z y_r$ is the Jacobian operator. An equation for Γ is obtained upon multiplying Eq. (3.2) by r , i.e.,

$$\Gamma_t - r^{-1}J(\psi, \Gamma) = \nu[r(r^{-1}\Gamma_r)_r + \Gamma_{zz}]. \quad (3.9)$$

The result of substituting Eqs. (3.6a) and (3.6b) into Eq. (3.5b) is

$$\eta = r^{-1}\psi_{zz} + (r^{-1}\psi_r)_r. \quad (3.10)$$

Eqs. (3.8)–(3.10) constitute the basic system of three equations in the three unknowns ψ , Γ and η .

The boundary conditions are of crucial importance for the successful simulation of the laboratory data. The following set of conditions allow solutions which agree well with Ward's data. Fig. (3.1) contains a map of the domain, the grid-point mesh and boundary

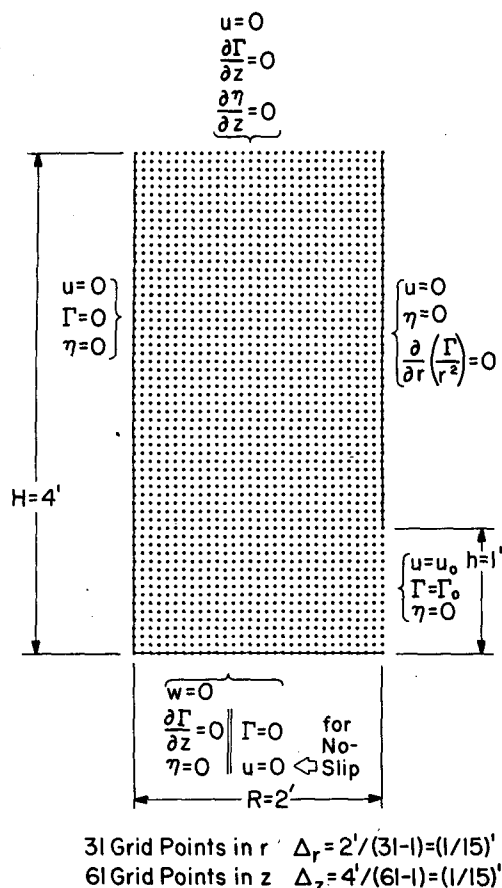


FIG. 3.1. The computation domain. A rectangular grid of equally spaced points is used for all experiments except those where frictional lower boundary conditions are used. In that case, $\Delta z = \frac{1}{2} \Delta x$.

conditions used. The boundary conditions are as follows:

1) $u = \eta = \Gamma = 0$ for $r = 0$ and $0 \leq z \leq H$. Symmetry requires there be no radial motion at the center ($u = 0$). The azimuthal vorticity $\eta = -w_r$ at $r = 0$ since u is zero for all z (i.e., $u_z = 0$). Again symmetry requires $-w_r = \eta = 0$ at $r = 0$. If Γ were any number other than zero at $r = 0$, v would be infinite here.

2) $w = \eta = \Gamma_z = 0$ for $z = 0$ and $0 \leq r \leq R$. The lower surface is impermeable ($w = 0$). The azimuthal vorticity $\eta = u_z$ since w is zero for all r (i.e., $w_r = 0$). Requiring the shear stresses (which are proportional to u_z and v_z , respectively) to vanish is equivalent to demanding $\eta = \Gamma_z = 0$. This (free-slip) condition allows the isolation of the updraft-swirl interaction since in this case boundary-layer-associated vorticity is absent. Section 7 presents some preliminary calculations using the non-slip conditions $w = u = \Gamma = 0$ at $z = 0$.

3) $u = \Gamma_z = \eta_z = 0$ for $z = H$ and $0 \leq r \leq R$. We require the flow to have no radial component as it exits ($u = 0$). We also require approximate cyclostrophic balance as the flow exists. Consider the diffusion term in Eq. (3.1).

Using the Eqs. (3.4) and (3.5b), it is easy to show

$$[r^{-1}(ru)_r]_r + u_{zz} = \eta_z.$$

Since u is zero at $z = H$ and it is expected that the term wu_z is small, requiring that η_z be zero leads to cyclostrophic balance. The condition $\Gamma_z = 0$ (free-slip) is unfaithful to the laboratory experiment since the honeycomb removes rotation from the outgoing air. The condition $\Gamma = 0$, however, leads to the development of an upper boundary layer which requires fine grid resolution. After carrying out integrations with both conditions, it became clear that since this condition has only a slight effect on the general results, the following solutions all have $\Gamma_z = 0$ at $z = H$.

4) $u = u_0$, $\Gamma = \Gamma_0$, $\eta = 0$ for $r = R$ and $0 \leq z \leq h$. The radial inflow and circulation are specified at $r = R$. This is equivalent to specifying the inflow angle $\alpha\{\tan^{-1}[v(R)/u(R)]\}$. The condition $\eta = 0$ is of paramount importance. A previous investigation (Harlow and Stein, 1974) used $w = 0$ at the inflow. That leaves η unspecified and hence nonzero. Thus, an unspecified amount of azimuthal vorticity is advected into the domain and the effect is profound [witness the difference between the results of present calculations and the Harlow-Stein (1974) model]. Physically, the vertical velocity is zero at the rotating screen but becomes non-zero as the edge of the exhaust radius is approached (which is where the model domain begins).²

5) $u = (r^{-2}\Gamma)_r$, $\eta = 0$ for $r = R$ and $h < z \leq H$. A fictitious impermeable wall is placed here ($u = 0$). This corresponds to the observational fact that the converging layer of warm moist air is of limited height (Davies-Jones (1976)). The last two conditions are manifestations of the free-slip condition.

The initial conditions in all the experiments are $\eta(r, z) = 0$, $\psi = \psi(r, z)$, which is the solution of Eq. (3.10) with $\eta = 0$ and $\Gamma(r, z) = 0$ for all r, z except at $r = R$ and $0 \leq z \leq h$ where Γ is specified. The next section describes the time evolution of this state.

The numerical method used to solve Eqs. (3.8)–(3.10) is straightforward. The spatial differencing has second-order accuracy. The nonlinear terms are differenced using the schemes of Arakawa (1966). The Euler method is used for the first time step; thereafter the leapfrog technique is employed. Viscous terms are lagged one time step. Averaging among time levels was performed every 20 time steps to avoid mode splitting. The time step chosen satisfies the CFL (Courant-Freidricks-Lewy) and diffusive stability criteria throughout the integration.

The majority of the experiments used the eddy viscosity $\nu = 1.86 \text{ cm}^2 \text{ s}^{-1}$ ($0.002 \text{ ft}^2 \text{ s}^{-1}$); the molecular viscosity of air is approximately $0.139 \text{ cm}^2 \text{ s}^{-1}$ (0.00015

² This point was also verified experimentally by the author on a recent visit to the University of Oklahoma where Ward's model is currently being used.

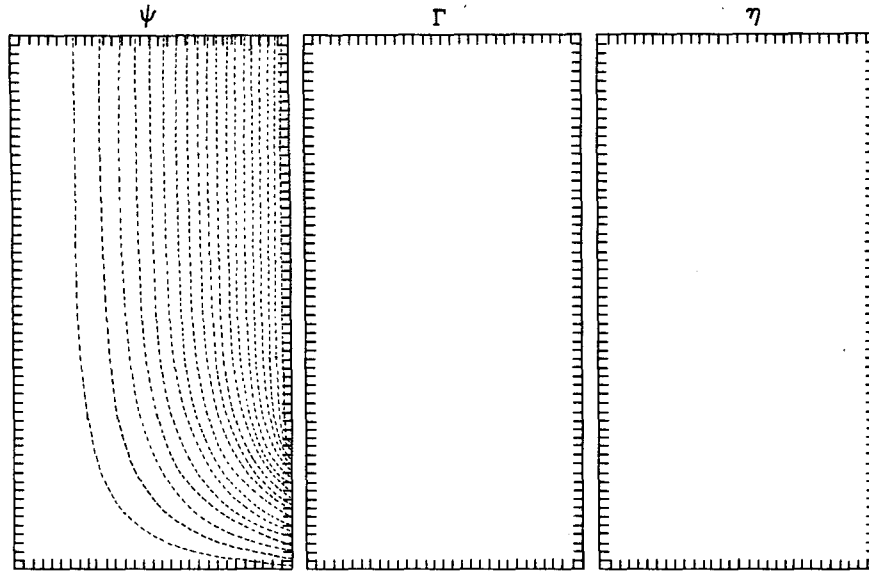


FIG. 4.1. The initial conditions for all experiments. The vorticity and circulation are zero everywhere; the streamlines are derived from Laplace's equation ($\nabla^2\psi=0$). This figure and the three subsequent figures detail the time evolution of the solution for $N=1000$ and $\alpha=22^\circ$. In this and all subsequent contour plots, dashed lines signify negative values. The specified inflow velocity is the constant u_0 , hence $\psi(R,z)=Ru_0z$ for $0\leq z\leq h$. In all experiments $u_0=-1.0$ ft s $^{-1}$ and $R=2$ ft, thus $\psi(R,z)=-(2.0\text{ ft}^2\text{ s}^{-1})z$ for $0\leq z\leq h$ and is $-(2.0\text{ ft}^2\text{ s}^{-1})h$ for $z\geq h$. Since $h=1.0$ ft, $\psi_{\min}=-2.0\text{ ft}^2\text{ s}^{-1}$. ψ is contoured in intervals of $0.1\text{ ft}^2\text{ s}^{-1}$ starting from the zero value at the axis and lower boundary.

ft 2 s $^{-1}$). Section 5 contains the results of varying ν over a very wide range. The inflow velocity u_0 is 30.5 cm s^{-1} (1 ft s^{-1}) for all experiments. Hence $N=u_0R/\nu=10^3$ for most experiments.

Ward found that two basic parameters governed the core size—the “configuration ratio” and the inflow angle α . Later, Davies-Jones (1973) reanalyzed Ward's data and found that the core size is solely a function of the swirl ratio S . The swirl ratio is related to the configuration ratio and the inflow angle in the following way. In Section 1 S was defined as $R\Gamma(R)/(2Q)$, but since $\Gamma(R)=Rv_0$ and $Q=Rhu_0$,

$$S = \frac{R}{2h} \frac{v_0}{u_0}. \quad (3.11)$$

Since the configuration ratio $c \equiv 2R/h$ and $v_0/u_0 = \tan\alpha$,

$$S = (c/4) \tan\alpha. \quad (3.12)$$

In the majority of the experiments $c=4$; hence the swirl ratio is simply the tangent of the inflow angle.

4. Time evolution

The initial ψ , Γ and η are shown in Fig. 4.1. Air enters from the right, turns and exits out the top. The flow is irrotational. Notice the vertical velocity ($-r^{-1}\psi_r$) is not zero at the entrance. The vertical velocity field is displayed in Section 6 and it appears that $w \approx z$ at $r=R$. This is simply the solution for an

irrotational solenoidal flow near a stagnation point (see Batchelor, 1967, p. 105). Since the streamfunction $\psi = -kzr^2/2$, $u = -kr/2$ and $w = kz$ in that case. The classical solution differs from the one shown in Fig. 4.1 at and above the height $z=h$ since we demand that $u=0$ at $z=H$.

Incidentally, if we assume v is independent of z and use these values of u and w , we can integrate Eq. (3.2) twice to obtain the result

$$\Gamma = \Gamma_\infty [1 - \exp(-kr^2/4\nu)]. \quad (4.1)$$

This solution for (u,v,w) is known as the Burgers-Rott vortex (see, e.g., Lewellen, 1976). Since Γ is independent of z in this solution there is no interaction between the swirl and the meridional motion [see Eq. (3.8)]. We shall see that this interaction is of crucial importance in the determination of the vortex core radius (to be defined). However, the Burger-Rott solution is useful for zeroth-order considerations. We shall next consider the time evolution of the state described by Fig. 4.1.

The azimuthal velocity at $r=R$ and $0\leq z\leq h$ is increased to a value of 12.19 cm s^{-1} (0.4 ft s^{-1}) ($\alpha=22^\circ$, in this example). Fig. 4.2 shows the solution at $t=5.0$ s. The circulation imposed by the rotating screen is being advected into the domain. A “front” of nonzero Γ advances into the previously nonrotating fluid. Ahead of the front $\Gamma=0$, while behind the front $\Gamma \approx \Gamma_0$ (the entrance value). The front slants from the lower left to the upper right implying $(\Gamma^2)_z < 0$. Therefore, by Eq. (3.8) we find that $\eta_t < 0$. Since η is initially zero,

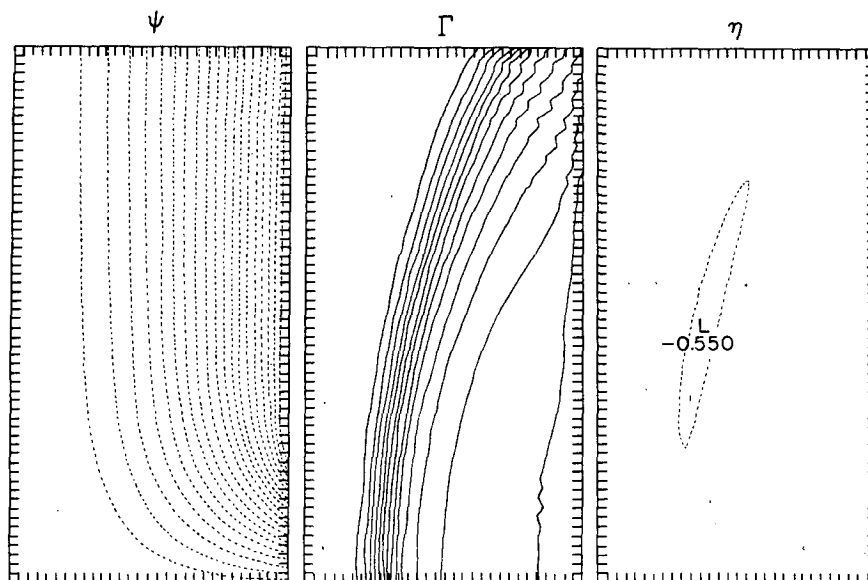


FIG. 4.2. The streamfunction, circulation and azimuthal vorticity at $t = 5.0$ s. Since $\alpha = 22^\circ$ and $|u_0| = 1.0 \text{ ft s}^{-1}$ $\Gamma(R, z) = 0.8 \text{ ft}^2 \text{ s}^{-1}$ for $0 \leq z \leq h$. Γ is contoured in intervals of $0.06 \text{ ft}^2 \text{ s}^{-1}$ starting from the zero value at the axis. η is zero at the left, right and lower boundary and is initially zero at the upper boundary. The contour interval is 1 s^{-1} starting at a value slightly greater than the minimum.

$\eta(t) < 0$ and has its minimum centered near the position of the maximum slope of the front. The magnitude of η at this time is insufficient to induce any perceptible change in the streamline pattern.

Fig. 4.3 indicates the front has advanced further inward and has a lessened vertical derivative. The azimuthal vorticity, however, has increased due to the factor r^{-3} multiplying $(\Gamma^2)_z$ in Eq. (3.8). A most interesting development occurs in the streamline field;

the zero streamline separates from the lower rigid surface and reattaches on the center axis. In this region enclosed by the zero streamline, downflow occurs near the axis.

The separation of the zero streamline is a necessary feature of the solution in a slightly viscous fluid. Consider a fluid parcel entering with an amount of angular momentum (rv). Since (in a slightly viscous fluid) the angular momentum is conserved, v increases

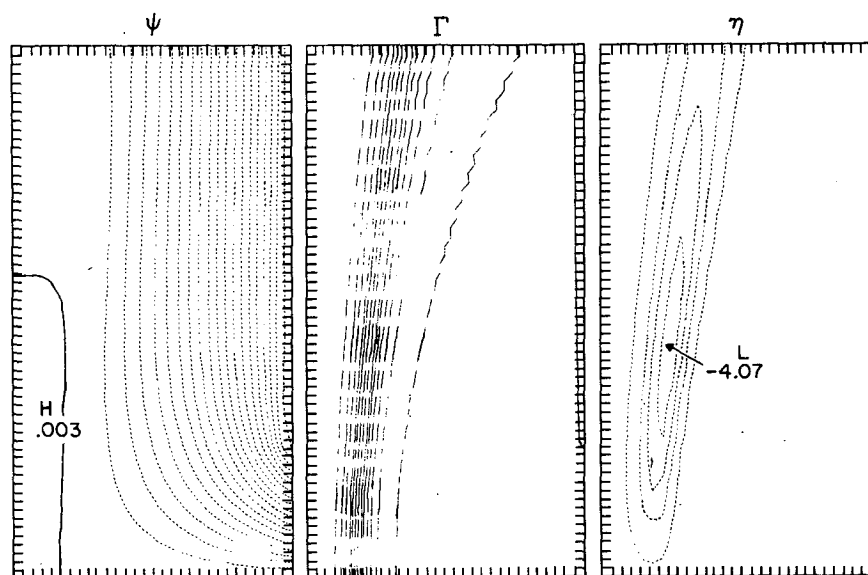
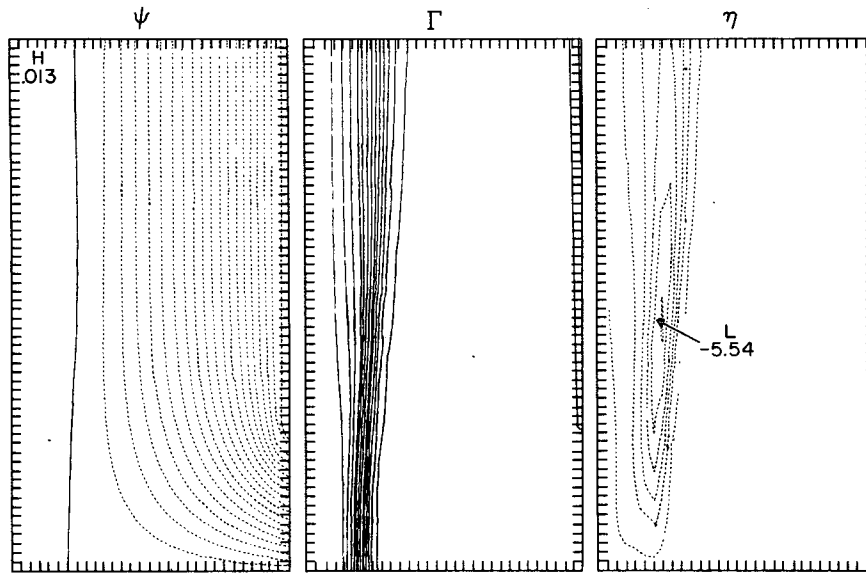


FIG. 4.3. As in Fig. 4.2 at $t = 7.0$ s. Note that ψ becomes positive with the area enclosed by the zero streamline. The relative high indicates downflow along the axis.

FIG. 4.4. As in Fig. 4.2 except at $t=30.0$ s.

as the parcel approaches the axis. When v increases to a degree where the outward centrifugal force balances the applied inward pressure gradient, radial motion must cease. But the parcel must continue to move because new air is continually being supplied at $r=R$ and the only way for it to move is up. In a more viscous fluid, a parcel can approach the axis while its angular momentum is diffused outward. The next section examines this process in more detail.

The steady-state solutions ($t=30.0$ s) are displayed in Fig. 4.4. These patterns are essentially unchanged after approximately $t=17.0$ s. A further check was

made by computing the flux of Γ out the top and comparing this to the exactly known influx of Γ .

For the remainder of this paper we refer to the zero streamline which separates from the floor as the core boundary. This is consistent with Ward's experimental definition, since he determined the core size by releasing smoke near $r=z=0$. Save for some diffusion the smoke mixing ratio S_{mr} obeys a steady-state equation $J(\psi, S_{mr})=0$ with the solution $S_{mr}=S_{mr}(\psi)$. Since the zero streamline passes through $r=z=0$, it is clear that the separated zero streamline can be identified with the "core" as defined by Ward.

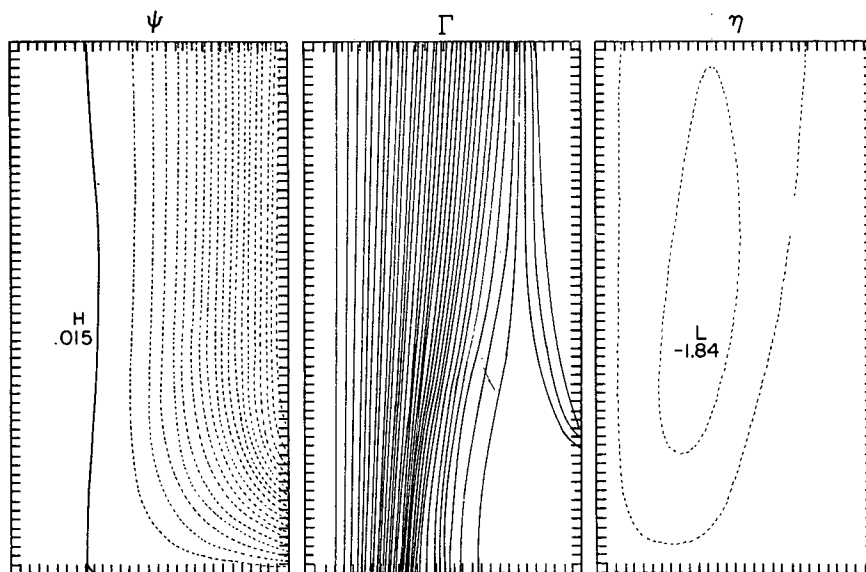


FIG. 5.1. The steady-state patterns of ψ , Γ and η for $N=50$ and $\alpha=45^\circ$. Since $\alpha=45^\circ$ and $|u_0|=1.0$ ft s^{-1} , $\Gamma(R,z)=2$ ft² s^{-1} for $0 \leq z \leq h$. The same contour intervals as those in Figs. 4.1–4.4 are used here and in Fig. 5.2. Note how diffuse the Γ field is.

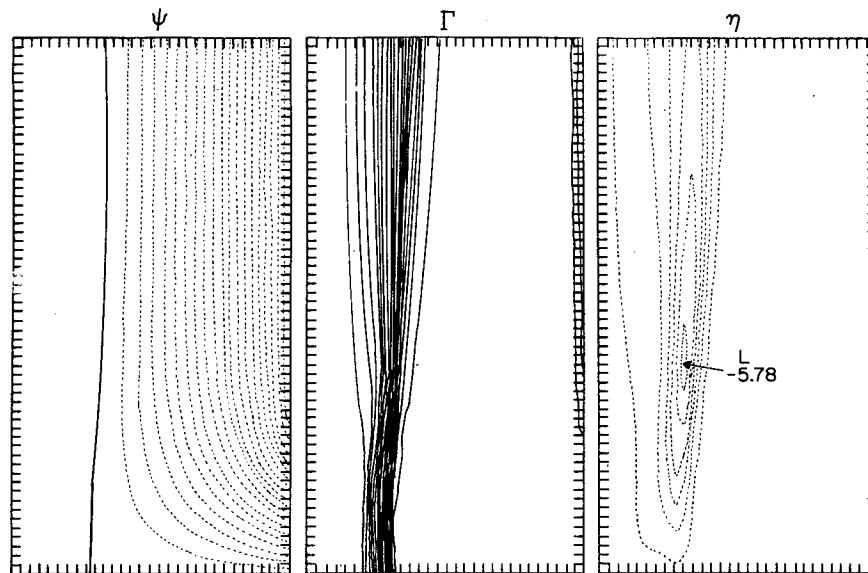


FIG. 5.2. The steady-state patterns of ψ , Γ and η for $N=1000$ and $\alpha=45^\circ$. The radial gradient of Γ (and, consequently η) is concentrated within a narrow region. Note the enlargement of the core over that in Fig. 5.1.

5. Comparison of experiments with different eddy viscosity

Lilly (1969), Ward (1972) and Davies-Jones (1973) argued that the main features of the tornadic circulation could be explained in terms of inviscid fluid dynamics. This section evaluates the role played by viscous

diffusion in the laboratory model through a series of simple tests.

Using an inflow angle $\alpha=45^\circ$, we vary ν through several orders of magnitude and investigate the effect on the steady-state solution. Fig. 5.1 shows the solution for $N=50$. The circulation is very diffuse; accordingly,

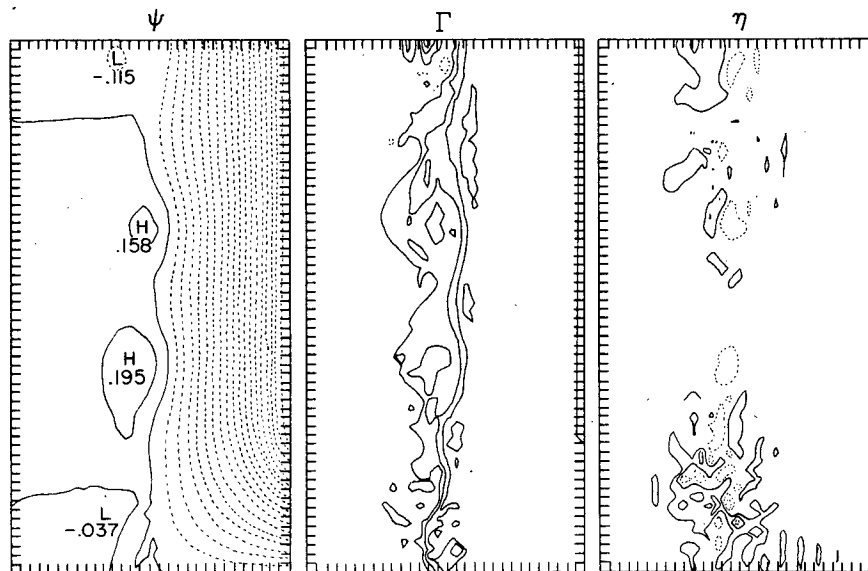


FIG. 5.3. The steady-state patterns of ψ , Γ and η for $N=1.3 \times 10^4$ and $\alpha=45^\circ$. This value of N comes from using the molecular viscosity of air at room temperature. Although the patterns exhibit many small-scale irregularities, the large-scale features such as the core size and the concentration of vorticity in the core wall persist. Γ is contoured every $0.6 \text{ ft}^2 \text{ s}^{-1}$ while η is contoured every 11.0 s^{-1} . The reason for this is that small-scale streamfunction variations when twice differentiated (to get vorticity) yield locally large values. The essential feature is that the vorticity is significantly nonzero only along the core.

the negative azimuthal vorticity is widely spread throughout the domain. Note the core size.

Increasing N to 1000 (Fig. 5.2) shows the transition between the inner region ($\Gamma \approx 0$) and the outer region ($\Gamma \approx \Gamma_0$) to be quite narrow. Notice the azimuthal vorticity is confined to a narrow sheet; in fact, all *three* components of vorticity are nonzero only within this narrow region. Fig. 5.3 further illustrates this behavior. Although the small-scale features are terribly messy, the larger scale features are essentially the same as observed in Fig. 5.2. That is, the core size is the same, and a concentrated vortex sheet exists which separates an inner region of almost stagnant flow from an outer region of irrotational ($\Gamma \approx \Gamma_0$) flow. Fig. (5.6) summarizes the behavior of the core radius as a function of N . The reason why the large-scale features persist in the limit of very small viscosity is as follows.

The type of flow which tends to develop as the steady-state solution in the small viscosity limit is shown schematically (Fig. 5.4). There are two regions: the inner region has $\Gamma = 0$ and $w = -W_0$. The flow is irrotational except at the discontinuity which separates the two flow regimes. The stability of such a flow to axisymmetric perturbations δ can be easily investigated by standard techniques (Rotunno, 1977). A general criterion for the stability of axisymmetric disturbances was derived by Howard and Gupta (1962). A Fourier decomposition of δ is made and the solution for a Fourier component $\delta_{\gamma, \sigma} e^{i\gamma z + i\sigma t}$ is obtained. The quantity σ is related to the axial wavenumber γ , ω_0 and Γ_0 through a dispersion equation $\sigma = \sigma(\gamma; W_0/V_0)$. For certain values of γ and W_0/V_0 , σ is real indicating the

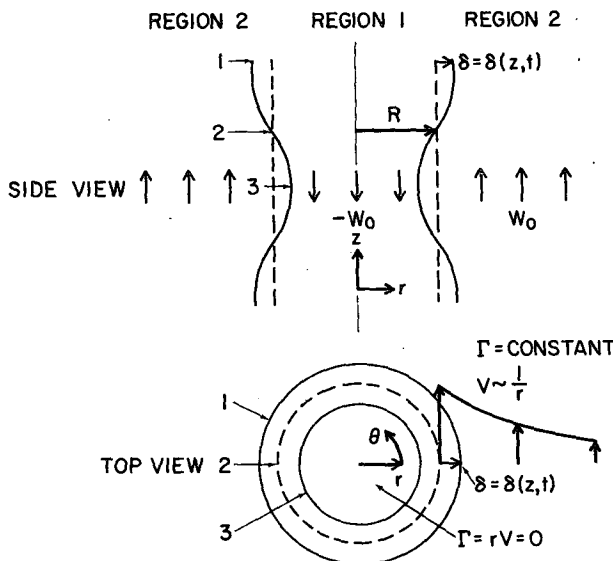


FIG. 5.4. Idealized flow believed to be attained in the inviscid limit. Region 1 contains a uniform downdraft with no azimuthal motion. Region 2 contains a uniform updraft and its azimuthal velocity is proportional to r^{-1} . Here $\delta = \delta(z, t)$ represents an axisymmetric perturbation of the material surface separating the two regions.

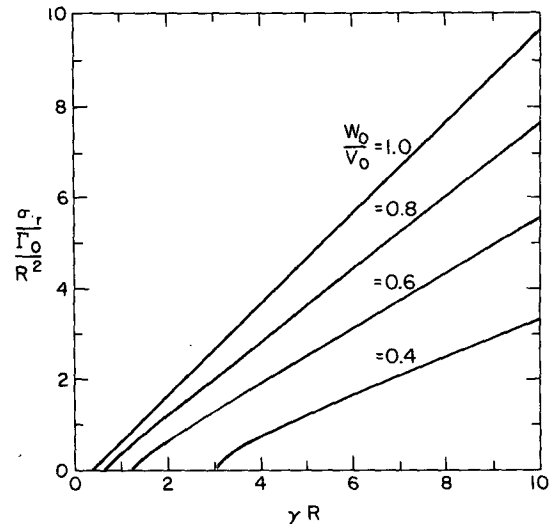


FIG. 5.5. The results of a stability analysis of the flow shown in Fig. 5.4. The perturbation $\delta(z, t)$ behaves as $e^{i\gamma z + i\sigma t}$; σ_r is the real part of σ and represents the rate at which unstable perturbations grow. The quantity γ is the axial wavenumber. Note that for γ small enough the perturbation is stable.

mode is unstable. The real part σ_r of σ is the growth rate. Fig. 5.5 is a graph of the growth rate versus axial wavenumber for increasing values of the parameter W_0/V_0 . Notice the low wavenumbers are stabilized by the rotation while the small wavenumbers are destabilized by the radial shear of the vertical velocity. Hence, Fig. 5.5 indicates that the large-scale features of the solution are preserved, but the small-scale instabilities cause considerable wrinkling of the core wall. A slight increase of ν damps these small waves but does not alter the basic circulation Γ to a degree where the core size is changed. The value of $\nu = 1.86 \text{ cm}^2 \text{ s}^{-1}$ ($0.002 \text{ ft}^2 \text{ s}^{-1}$) was chosen to achieve this goal.

Ward (1972) observed the formation of multiple vortices when the swirl ratio exceeds a certain value. Ward (1972) and Davies-Jones (1973, 1976) have

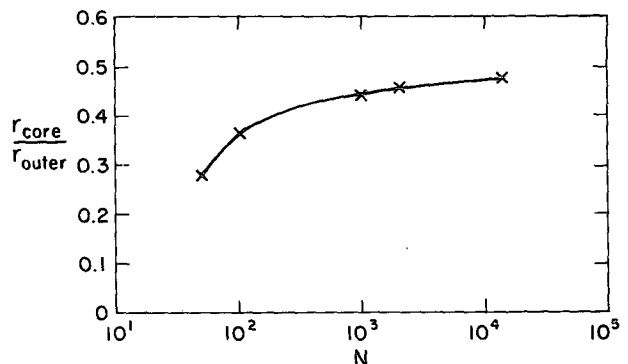


FIG. 5.6. Average core size versus Reynolds number. The radial position of the separated zero streamline varies slightly with height. Hence the crosses represent half the sum of the outermost and innermost position of the zero streamline. For these experiments $\alpha = 45^\circ$.

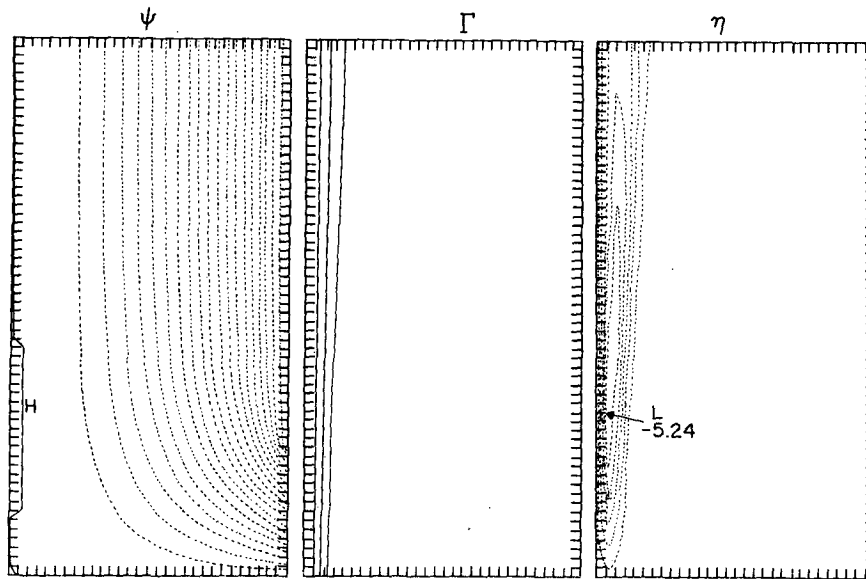


FIG. 6.1. The steady-state patterns of ψ , Γ for $N=1000$ and $\alpha=6^\circ$. The same contour intervals as those in Figs. 4.1–4.4 are used here and in Fig. 6.2

attributed these vortices to an instability of a cylindrical vortex sheet. Since the present model is axisymmetric, it is impossible to simulate this phenomenon. However, the fact that the axisymmetric model tends toward a cylindrical vortex sheet configuration lends support to their hypothesis.

6. Comparison with Ward's data

The section contains a comparison of the numerical and laboratory data. Specifically, we wish to compare the effects of varying the imposed swirl on the core

size. A further test is provided by comparing the numerical with the laboratory surface pressure patterns. Since Ward used no internal probes, quantitative flow comparisons are not possible.

The steady-state solution for $\alpha=0^\circ$ is the same as that shown in Fig. 4.1. The steady-state solutions for $\alpha=6^\circ$ and 45° are shown in Figs. 6.1 and 6.2, respectively. The core size increases with increasing α . Accordingly the “front” in the circulation field and the negative vorticity maximum move further away from the axis with increasing α . These results are summarized in Fig. 6.3 where the core radius as a

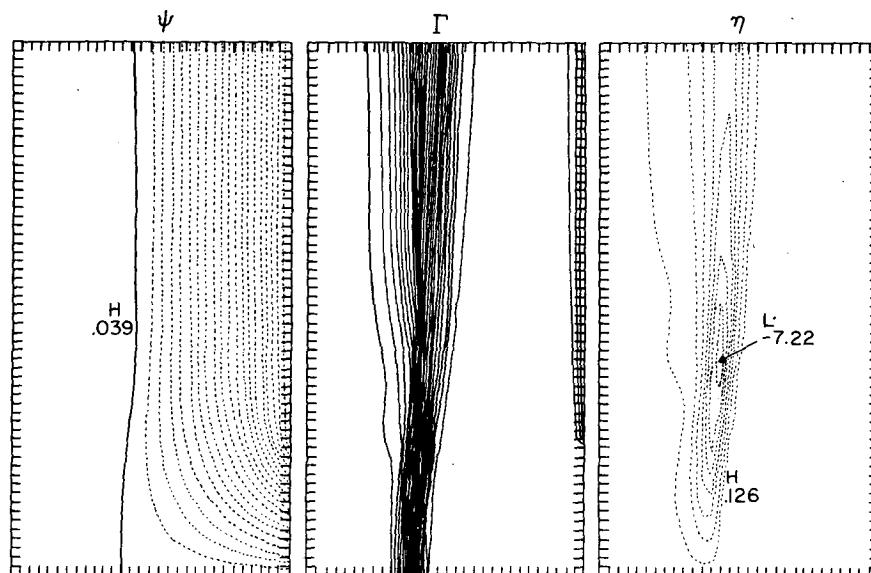


FIG. 6.2. The steady-state patterns of ψ , Γ and η for $N=1000$ and $\alpha=45^\circ$. The same contour intervals as those in Figs. 4.1–4.4 are used here.

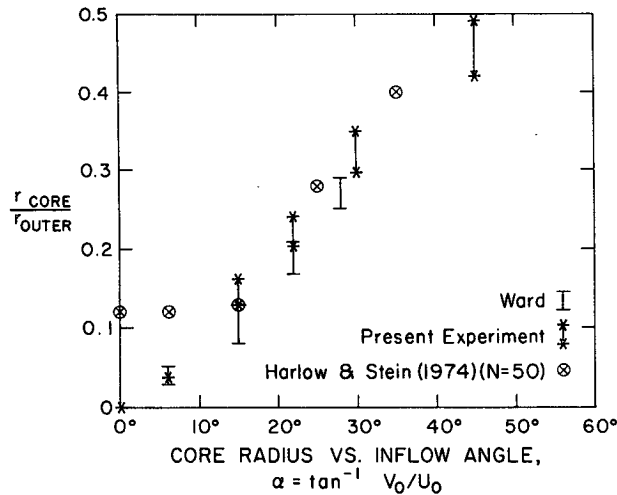


FIG. 6.3. Nondimensional core radius versus inflow angle. Ward's data correspond to a configuration ratio $c=4$. The size of the vertical bars is a measure of the scatter in the data. The size of the vertical bars for the present experiment (with $N=1000$) is a measure of the vertical variation of the core boundary. The crossed points are taken from Figs. 19 and 20 of Harlow and Stein (1974) which use $N=50$.

function of inflow angle is plotted. Also in the same graph are Ward's experimental values and the results of a previous modelling attempt (Harlow and Stein, 1974). The present model differs from the Harlow and

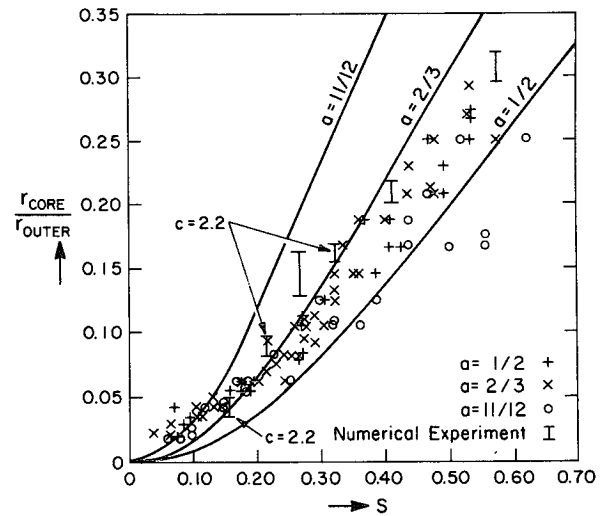


FIG. 6.5. Nondimensional core radius versus swirl ratio (after Davies-Jones, 1973). The parameter a is the aspect ratio h/R . Solid curves are $r_{core}/R = \sin^2 \theta$ (a theoretical relationship derived by Ward) for the different a . The data plotted in this way indicate the core radius is solely a function of S . The bars represent cases from the numerical experiment using $c=4$ and 2.2.

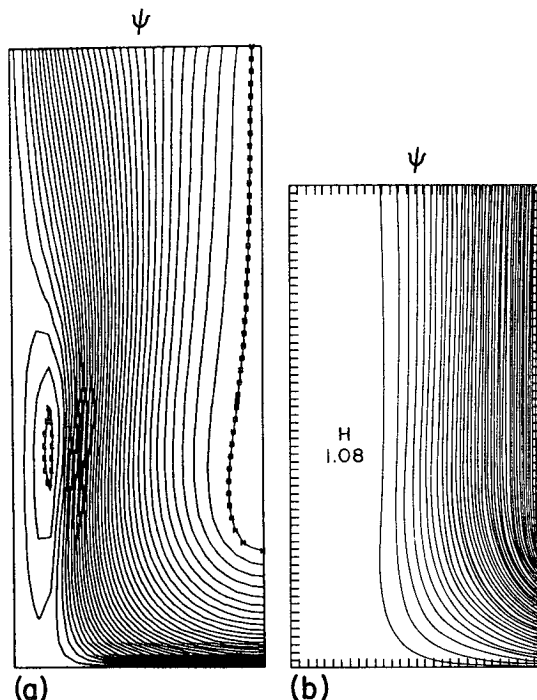


FIG. 6.4. Steady-state pattern of the logarithm of ψ for the case $c=4$, $N=50$ and $\alpha=45^\circ$. The left-hand contour plot is after Harlow and Stein (1974), where the condition $w=0$ at $r=R$, $z \leq h$ is used rather than $\eta=0$ at $r=R$, $z \leq h$ which is used in the present model (the right-hand contour plot).

Stein (HS) model in two aspects. As mentioned in Section 3, we require $\eta=0$ on the inflow boundary while HS require $w=0$. The other difference is we use a much lower viscosity for our comparisons with Ward's data. Fig. 6.4 is a comparison of the steady-state streamline pattern (the logarithm of $(\psi+a \text{ constant})$ is plotted for comparison with HS) for the case $c=4$, $N=50$ and $\alpha=45^\circ$. The nondimensional position of the recirculating cell's center in the HS result is 0.139 while the present model's is 0.241. We believe the reason for this is as follows. We have demonstrated in Section 4 that the vertical gradient of Γ produces negative η which induces the central downdraft. The HS model inflow boundary appears to have $w_r < 0$ and hence, $\eta = -w_r > 0$. Thus, it seems the flow must penetrate further inward in the HS model before the term $r^{-3}(\Gamma^2)z$ in Eq. (3.8) can counteract the effect of the inward positive η advection from the boundary. Note also the core boundary in the present model exhibits much less vertical variation. HS define the core as the eleventh streamline away from the center-low of the recirculating cell because this leads to the best fit with Ward's data. However, as Fig. 6.3 indicates, consistent application of this criterion leads to a nonzero core radius even when $\alpha=0^\circ$.

Note that our core size is slightly larger than the laboratory data indicate. We will show in the following section, however, that the incorporation of some type of frictional lower boundary condition tends to decrease the core size for a given α .

Davies-Jones (1973) replotted Ward's data and found the core size depends solely on the swirl ratio. Using Eq. (3.12), we can put our data from the two experiments using different c on Davies-Jones graph

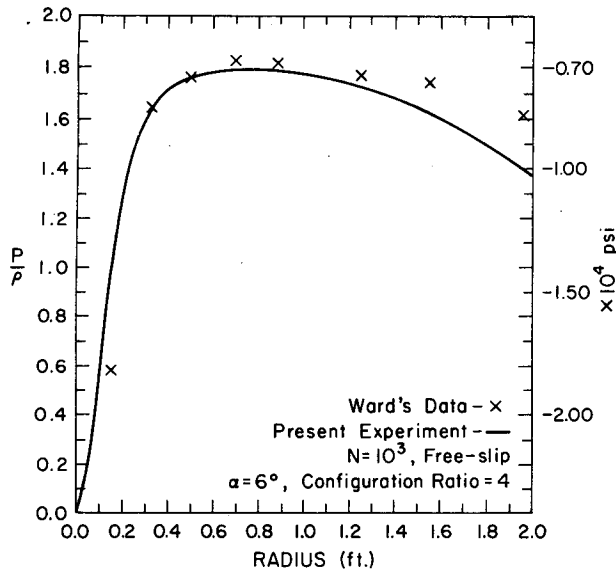


FIG. 6.6. Surface pressure versus radius. The solid line represents the numerical data for $N=1000$ and $\alpha=6^\circ$. The crosses are data points measured by Ward for $\alpha=6^\circ$. Note the relative high in pressure occurs for all practical purposes at the same radius in the numerical and laboratory experiments.

(Fig. 6.5). These results lend further support to the notion that the core size is a function only of S .

Fig. 6.6 shows the close agreement between the numerical and laboratory surface pressure patterns. The high-pressure "ring" is a characteristic feature of the vortex. The steady-state inviscid form of Eq.

(3.1) along the lower surface ($z=0$) is

$$\left(\frac{u^2}{2}\right)_r - \frac{v^2}{r} = -\frac{1}{\rho} P_r = -\frac{\partial P}{\partial r}. \quad (6.1)$$

In Section 4, we noted that the initial meridional flow is similar to the classical irrotational corner flow. The solutions shown above indicate the flow outside the core remains similar to the classical solutions. The tangential flow outside the core is irrotational ($v \approx r^{-1}$). Hence, approximate forms for u and v are

$$u = -\frac{r}{R} u_0, \quad v = -\frac{R}{r} v_0, \quad (6.2a,b)$$

where u_0 and v_0 are defined in Section 3. We substitute these into Eq. (6.1) to obtain

$$\frac{u_0^2}{R^2 r^3} \left(r^4 - R^4 \frac{v_0^2}{u_0^2} \right) = -\frac{P_r}{\rho},$$

or using Eq. (3.12) with $c=4$,

$$P_r \sim \left(\frac{r}{R} \right)^4 - S^2. \quad (6.3)$$

We know that for small r Eq. (6.3) does not apply and that the pressure increases with increasing radius ($P_r > 0$). For a local pressure maximum the pressure must begin to decrease beyond some radius. Eq. (6.3)

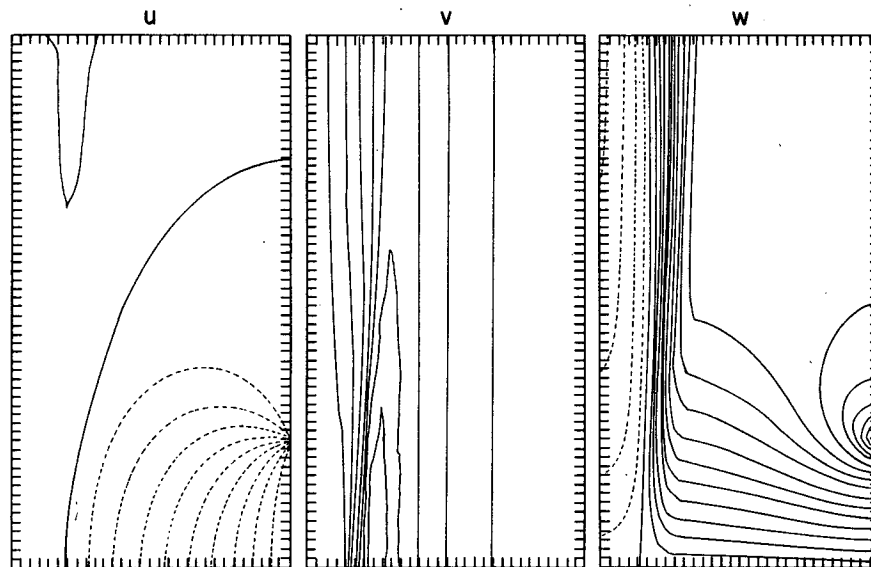


FIG. 6.7. The steady-state patterns of u , v and w for $N=1000$ and $\alpha=22^\circ$. The solid line cutting across the u contour plot is the zero line to the right of which the flow is inward and decelerating from the inlet value of -1.0 ft s^{-1} . The contour interval is 0.1 ft s^{-1} . The v field is contoured every 0.2 ft s^{-1} , starting with the zero axis value v increases outward until the core is reached, then v decreases as r^{-1} to the inlet value of 0.4 ft s^{-1} . The solid line separating the dashed and solid lines in the w contour plot is the zero velocity line. The w field is contoured every 0.1 ft s^{-1} .

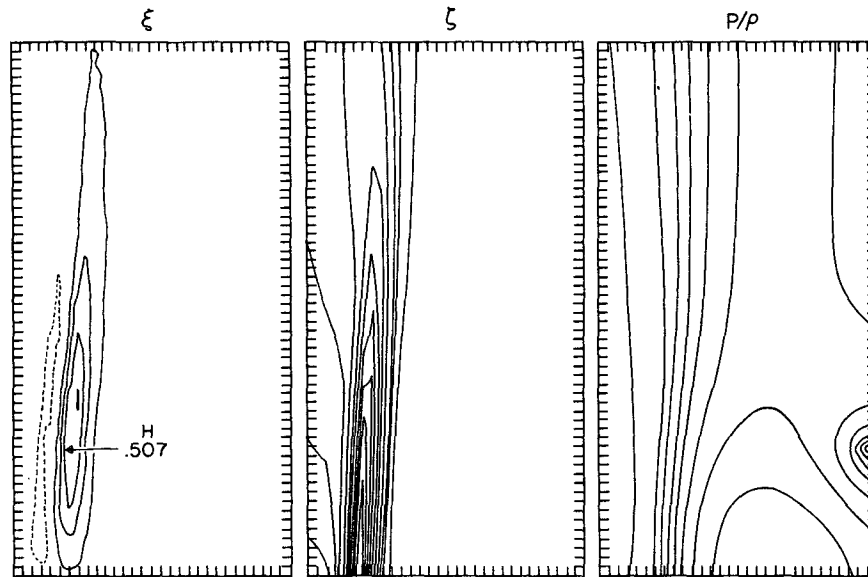


FIG. 6.8. The steady-state patterns of ξ , ζ and P/ρ for $N=1000$ and $\alpha=22^\circ$. The ξ field is contoured every 0.15 s^{-1} and the ζ field is contoured every 1.0 s^{-1} and reaches a maximum of approximately 10.0 s^{-1} in the core wall. The P/ρ field is computed relative to a value of zero at $r=z=0$. The first line from the axis is a zero line and hence $P/\rho < 0$ between the axis and this line. The P/ρ field is contoured in intervals of $0.2 \text{ ft}^2 \text{ s}^{-2}$. Note the relative maximum near the surface.

indicates that that radius is $r=RS^{\frac{1}{2}}$. Clearly, for $S > 1$ the high pressure ring is outside the domain. To summarize, a parcel of air enters with a specified amount of angular momentum (rv). As r decreases, v increases and hence, an outward centrifugal force develops. When this outward force balances the inward inertial force, $P_r=0$. Thus, there exists a local pressure maximum (stagnation point) at that radius.

Other flow quantities of interest are displayed in Figs. 6.7 and 6.8. We consider the $\alpha=22^\circ$ case. Fig. 6.7 displays the radial, azimuthal and vertical velocity fields. Fig. 6.8 displays the radial and vertical vorticities and the pressure (divided by density ρ). Note again the concentration of vorticity in the core wall. The pressure minimum is displaced slightly off the axis. This is due to the fact that the inner downdraft which terminates at the lower surface is associated with a local stagnation point at $r=z=0$, the pressure lowers as the flow turns radially outward at the corner. Another relative minimum in pressure is associated with the strong updraft just outside the vortex core. Most investigators agree the tornado funnel is made visible by condensation which is induced by the lowered pressure in the center of the rotating flow. It sometimes occurs that tornadoes appear to have double walls [see for example, the beautiful work of Golden (1973)]. A possible explanation is as follows. Consider the steady-state solution for $\alpha=45^\circ$, $N=2000$ shown in Fig. 6.9. The interior condensation is induced by the lower center pressure due to cyclostrophic flow. The outer wall which is generally much lighter (thus we can see through it to

the inner wall) is condensation induced by the low-pressure associated with the large vertical velocity just outside the core. The fact that the outer wall is lighter than the inner wall is consistent with the model result that the pressure drop is less outside the core than within. These aspects are more apparent in the solutions with larger swirl ratios.

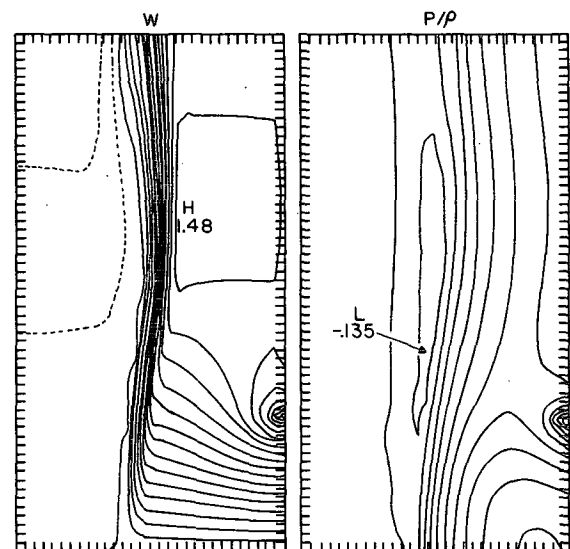


FIG. 6.9. The steady-state patterns of w and P/ρ for $N=2000$ and $\alpha=45^\circ$. The line enclosing the relative low (-0.135) is a zero line as is the first line away from the axis. The contouring is the same as in Figs. 6.7 and 6.8. This figure emphasizes the fact that there is a lowered pressure just outside the core wall which is associated with the intense updraft.

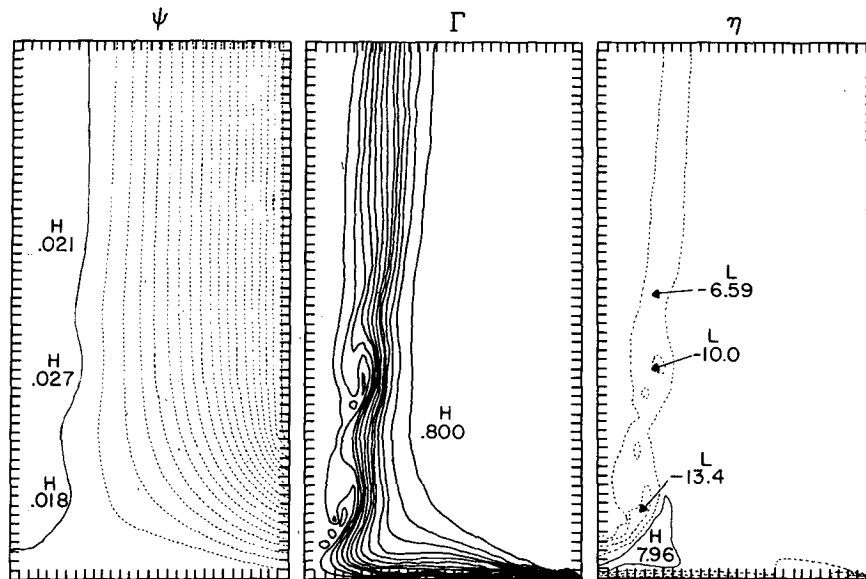


FIG. 7.1. The steady-state patterns of ψ , Γ and η for $N=1000$ and $\alpha=22^\circ$ using the no-slip conditions $u=v=0$ and $z=0$. In this and the following figure the contouring for ψ and Γ is the same as used in Figs. 4.1–4.4. However, due to the large boundary-layer induced vorticity, η is contoured in intervals of 6.0 s^{-1} . Note the wave structure.

7. Experiments with a no-slip lower surface condition

Although our investigation in this area is not complete, preliminary results are sufficiently interesting to be reported here. We investigate two types of non-slip conditions. The first is $u=v=0$ at $z=0$. Since the high laboratory Reynolds number leads to a very thin boundary layer, we have increased the vertical resolution in the following experiments by a factor of 2.

The Reynolds number used ($N=1000$) permits the proper resolution of the boundary layer. However, the laboratory Reynolds number may be much larger ($\sim 10^5$). Thus, the no-slip conditions $u=v=0$ at $z=0$ may be relevant only to a laminar flow. Maxworthy (1972) performs a vortex experiment which is largely in the laminar regime; some qualitative comparisons are made below.

The other condition was originally used by Taylor

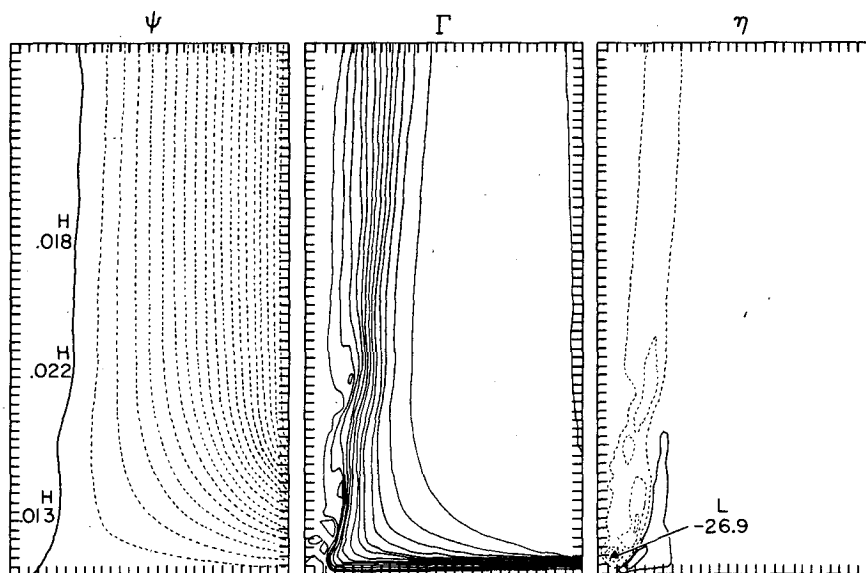


FIG. 7.2. The steady-state patterns of ψ , Γ and η for $N=1000$ and $\alpha=22^\circ$ using the Taylor conditions $(u,v) = K(u_z, v_z)$ at $z=0$ where $K=3.1 \text{ cm}$. The zero streamline now separates before the axis is reached and core undulations are less pronounced than in Fig. 7.1.

(1915) and more recently by Kuo (1971). It is required that $(u, v) = K(u_z, v_z)$ at $z=0$ which is regarded as the top of the turbulent surface layer. The condition is that the velocity and stress be in the same direction at the top of the turbulent surface layer. Note that when $K=0$ we recover the no-slip condition and when $K \rightarrow \infty$ we recover the free-slip condition. In the following example we choose $K=3.1$ cm.

Fig. 7.1 shows the solutions for $\alpha=22^\circ$ using the no-slip condition and increased vertical resolution. The most striking difference between this and the free-slip flow (Fig. 6.4) occurs in the lower left corner. The core wall now has a number of axial wrinkles which appear to be centrifugal waves. The time evolution indicates the lower wave develops first, then the upper wave; the axial phase does not shift throughout the integration. These standing waves appear to be breaking; notice how some lines of constant Γ form S shapes in the antinode of the wave. This indicates that (locally) $(\Gamma^2)_r < 0$ (Rayleigh's criterion for inertial instability).

The similarities between these results and the theory of vortex breakdown as advanced by Benjamin (1962) are immediately apparent. Benjamin likens the sudden enlargement of the vortex core to the sudden increase in depth of fluid flowing in an open channel under the influence of gravity (i.e., a hydraulic jump). Benjamin argues that in passing from a supercritical to a subcritical state, the flow force $(\frac{1}{2}w^2 + P/\rho)$ is increased. But to maintain a steady flow, the flow force must be the same on either side of the jump. Benjamin shows that the standing waves in the subcritical flow act to reduce the upstream flow force in such a way as to maintain a steady state. This description holds for weak jumps (i.e., a transition from a slightly supercritical to a subcritical state). For stronger transitions, dissipation occurs first in the form of breaking of the lead wave with nonbreaking standing oscillations downstream. Stronger transitions lead to breaking of the downstream waves. A structure very similar to that calculated in Fig. 7.1 is observed by Maxworthy (1972, Fig. 5a).

As remarked earlier, results using the no-slip condition for the Reynolds number used should only be compared with a laminar (at least upstream of the breakdown) flow. The flow in Ward's experiments is turbulent and does not show a strong resemblance to the flow of Fig. 7.1. Instead, Ward's flow appears much as the flow in Fig. 7.2. This figure contains the steady-state solutions for $\alpha=22^\circ$ with the Taylor conditions at the lower surface. Here, the zero streamline does not penetrate to the axis but separates as before. Undulations on the column are still present, but are not as pronounced as in Fig. 7.1. Notice that the same vertical resolution as in the free-slip cases can be used.

Experiments currently in progress are designed to examine more closely the flow in the corner region. Obviously, the flow in this region is of paramount importance, since in the atmosphere this is the region

of human habitation. A proper resolution of boundary layer processes is a key element in the understanding of the vortex as a whole.

8. Conclusions

Davies-Jones (1976) argues that Ward's (1972) laboratory experiment is more geophysically relevant than earlier models in that Ward's model exhibits both dynamic and geometric similarity to tornadoes. In view of this, it was decided that a numerical simulation of Ward's experiment would be a valuable precursor to a necessarily more sophisticated tornado model.

Using an axisymmetric constant density and viscosity model, we come to the following major conclusions.

1) The core size is mainly a function of the swirl ratio as argued by Davies-Jones (1973). This result is contingent on the proper specification of the azimuthal vorticity at the inflow boundary. A previous model left the inflow boundary value of η unspecified, and hence, severely altered the core size versus swirl ratio relationship.

2) The core size is independent of the Reynolds number for large Reynolds number. Varying the constant viscosity in a series of experiments indicates the core size does not change as the viscosity becomes very small (its molecular value). The core size obtained in the small viscosity limit is the one which best agrees with Ward's (1972) data.

3) These solutions lend support to the notion that the core is relatively stagnant and the outer flow moves irrotationally and that these two regions are separated by a thin region of high vorticity.

Preliminary calculations using frictional lower boundary conditions are reported. The frictional lower boundary appears to induce "vortex breakdown" as described by Benjamin (1962). Briefly, vortex breakdown is characterized by a sudden enlargement of the core with standing waves on the downstream (subcritical) side. Since Benjamin's (1962) theory does not treat the case where there is a solid boundary normal to the core axis (as we have), it is clear that additional work must be done to assess the relevancy of Benjamin's (1962) theory. Calculations of this nature are currently in progress.

Acknowledgment. The author wishes to thank Dr. D. K. Lilly for suggesting the problem and for some helpful discussions and comments concerning the manuscript.

REFERENCES

- Arakawa, A., 1966: Computational design for long-term numerical integration of the equations of fluid motion: two-dimensional incompressible flow. Part I. *J. Comput. Phys.*, **1**, 119-143.
- Batchelor, G. K., 1967: *An Introduction to Fluid Dynamics*. Cambridge University Press, 615 pp.

- Benjamin, T. B., 1962: Theory of vortex breakdown phenomenon. *J. Fluid Mech.*, **14**, 593-629.
- Davies-Jones, R. P., 1973: The dependence of core radius on swirl ratio in a tornado simulator. *J. Atmos. Sci.*, **30**, 1427-1430.
- , 1976: Laboratory simulations of tornadoes. *Preprints Symposium on Tornadoes*, Texas Tech University, 22-24 June, 151-174.
- Golden, J. H., 1973: The life cycle of the Florida Keys water spout as the Result of five interacting scales of motion. Ph.D. dissertation, Florida State University, 371 pp.
- Harlow, F. H., and L. R. Stein, 1974: Structural analysis of tornado-like vortices. *J. Atmos. Sci.*, **31**, 2081-2098.
- Howard, L. N., and A. S. Gupta, 1962: On the hydrodynamic and hydromagnetic stability of swirling flows. *J. Fluid Mech.*, **14**, 463-476.
- Kuo, H. L., 1971: Axisymmetric flows in the boundary layer of a maintained vortex. *J. Atmos. Sci.*, **28**, 20-41.
- Lewellen, N. S., 1971: A review of confined vortex flows. NASA Rep. CR-1772, 219 pp.
- , 1976: Theoretical models of the tornado vortex. *Preprints Symposium on Tornadoes*, Texas Tech University, 22-24 June, 107-144.
- Lilly, D. K., 1969: Tornado dynamics. NCAR manuscript 69-117.
- Maxworthy, T., 1972: On the structure of concentrated, columnar vortices. *Astro. Acta*, **17**, 363-374.
- Rotunno, R., 1977: A note on the stability of a cylindrical vortex sheet. Submitted to *J. Fluid Mech.*
- Taylor, G. I., 1915: Eddy motion in the atmosphere. *Phil. Trans. Roy. Soc. London*, **A215**, 1-126.
- Ward, N. B., 1972: The exploration of certain features of tornado dynamics using a laboratory model. *J. Atmos. Sci.*, **29**, 1194-1204.